Earth Planet. Sci. Lett. 626 (2024) 118535

Contents lists available at ScienceDirect

Earth and Planetary Science Letters

journal homepage: www.elsevier.com/locate/epsl

Miocene time-averaged geomagnetic field model suggests long lived mantle control and recurring structure in the South Atlantic

Y.A. Engbers [a,b,*], R. Holme [a], A.J. Biggin [a]

[a] Geomagnetism Laboratory, Department of Earth, Ocean and Ecological Sciences, University of Liverpool, Liverpool L69 7ZE, United Kingdom
[b] Electronic Defence, Netherlands Organisation for Applied Scientific Research (TNO), 2509 JG The Hague, the Netherlands

ARTICLE INFO

Editor by: Dr H Thybo

Keywords:
Time-averaged field
Inverse model
Miocene
Core-mantle boundary
Geomagnetic field structures

ABSTRACT

Reconstructions of long-term time-averaged geomagnetic field structures are important to understand geomagnetic field evolution and to identify the longevity and scale of non-dipolar field morphology. This study presents *MTAM1*, a non-zonal time-averaged field model for the Miocene era (5.3–23 million years ago), or indeed any time period prior to 5 million years ago. The time averaged field model for the Miocene is an inverse model based on a directional data compilation comprising 38 different localities, each with a minimum of 10 sites, called *PSVM* (Engbers et al., 2022a). The data were separated into normal ($PSVM_N$) and normalised reversed ($PSVM_R$) datasets, yielding two corresponding models $MTAM1_N$ and $MTAM1_R$. Allowing for the opposite sign, no substantial differences were found between these two models, suggesting symmetry between the morphology of the normal and reversed fields and no evidence for non-reversing features in the geomagnetic field. Under this assumption of symmetry, the normal and reversed data can be modelled together, enhancing the data distribution and thus the robustness of the complete time-averaged field model for the Miocene. The broad structure of the models resembles previous time-averaged field models for the past 5 Myr but there are some clear differences, particularly under the South Atlantic, where all Miocene models include a reversed flux patch (RFP). To investigate whether this difference is well defined, or could result from differences in modelling methodology or data distribution, the data of the last 5 Myr were inverted with our normal model for the Miocene as a prior constraint. We find no evidence that the Miocene model is inconsistent with the field structures required by data from the past 5 Myr, suggesting an overall stability in the averaged geomagnetic field morphology for the past 23 Myr. This is consistent with long-term mantle control on geomagnetic field morphology leading to consistent deviations from the geocentric axial dipole on a multi-million-year timescale on the Core-Mantle boundary (CMB).

1. Introduction

The magnetic field of the Earth is generated in the outer core. Convecting liquid iron supports a self-sustaining dynamo, referred to as the geodynamo. Palaeomagnetic records constrain the changes of strength and structure of the magnetic field through time but the observations are sparse in space and time as they are reliant on the presence of well-preserved rocks with stable magnetic carriers. It is common to assume that, when averaged over sufficient time, the magnetic field approximates to a geocentric axial dipole, or GAD (Evans, 2006; Opdyke and Henry, 1969). The questions remain: how good is this approximation and how much time is needed for it to apply? Time dependent models have been constructed to fit available data on a range of timescales, from the current field, to timescales of a few hundred years to 100kyrs (Alken et al., 2021; Constable et al., 2016; Jackson et al., 2000; Korte et al., 2009; Panovska et al., 2018; Thébault et al., 2015). For older times, data restrict calculation to the time-averaged field (TAF) such as LN3 based on the 0–5 Myr normal data from PSV10 (Cromwell et al., 2018). The further back in time, the sparser the available data, and also the more uncertain the palaeogeography: hence the lower the resolution of the models in both space and time. All of these field models show substantial common non-dipolar field structure (departures from GAD), including high-latitude patches of enhanced flux. Further, evidence supports that the South Atlantic Anomaly (SAA), an anomalously weak region of the

* Corresponding author at: Geomagnetism Laboratory, Department of Earth, Ocean and Ecological Sciences, University of Liverpool, Liverpool L69 7ZE, United Kingdom.
E-mail address: yaelengbers@gmail.com (Y.A. Engbers).

https://doi.org/10.1016/j.epsl.2023.118535
Received 29 June 2023; Received in revised form 3 November 2023; Accepted 5 December 2023
Available online 23 December 2023

field focused (today) on South America is only the most recent product of a recurrent anomalous feature in the South Atlantic region on a multi-million-year timescale (Engbers et al., 2020, 2022b; Nilsson et al., 2022; Panovska et al., 2019; Tarduno et al., 2015).

Here we investigate whether there is enough sufficiently well-distributed data coverage to go further back in time than the current 5 Ma to provide useful information on the morphology of the field. The dataset *PSVM* (Fig. 1, $PSVM^{\Delta I}$ in Engbers et al., 2022a) collects field measurements for the Miocene era based on palaeodirectional data from volcanic rocks that formed between 23 and 5.3 Ma. *PSVM* allows us to explore the geomagnetic TAF in the Miocene, to investigate whether the available measurements are sufficient to constrain the morphology of that TAF. The *PSVM* dataset in this study, is the same as $PSVM^{\Delta I}$ in Table 1 in Engbers et al. (2022a). The localities that experienced vertical axis block rotations have been excluded from the complete *PSVM* database for this study as was done for the inclination anomaly analyses in Engbers et al. (2022a). $PSVM^{\Delta I}$ contains 38 localities instead of the 44 that are available in the complete *PSVM* dataset. We used the selection criteria of $k > 30$ and $n \geq 3$, a minimum of 10 sites per locality ($N \geq 10$) and the Vandamme cutoff (Vandamme, 1994), as in selection criteria set 1 ($CS1_{vD}$) in Engbers et al. (2022a). This dataset is described as *PSVM* in the rest of this manuscript and is further described in the Supplementary Materials Section S1 and Supplementary Materials Table S1. It is important to note that the "chosen model" in Engbers et al. (2022a), was not $CS1_{vD}$, but $CS7_{vD}$ which explains all differences in the tables between these two studies. Specifically, more localities pass the selection criteria here, as different selection criteria were applied. We were able to be more lenient with data selection here as there is lower potential for bias from outliers here than in the individual VGP angular dispersion estimates produced by Engbers et al. (2022a).

The governing equations for the evolution of the geomagnetic field - the induction and Navier-Stokes equations (Matsushima and Honkura, 1992) are invariant to a change in sign of the magnetic field; which suggests that, averaged over sufficient time, normal and reversed field morphologies should match: models for the two states should differ only in their sign. However, it is not clear whether the data support this symmetry, or whether the normal and reversed fields might differ due to non-reversing features in the geomagnetic field. Previous spherical harmonic models of the time-averaged palaeomagnetic field have been created using only the more numerous normal data (e.g. LN3 (Cromwell

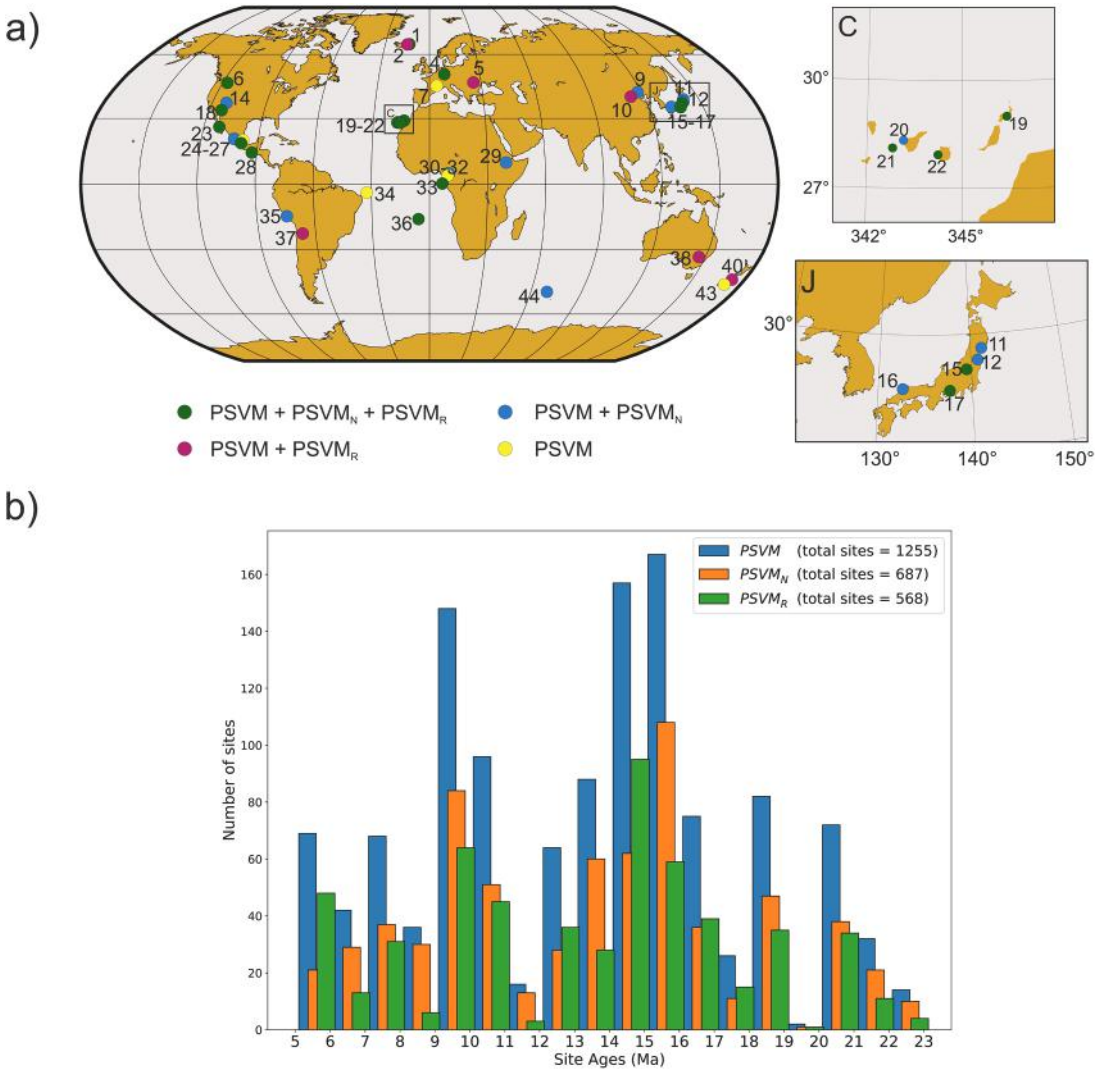

Fig. 1. General information on the *PSVM* dataset used in this study ($PSVM^{\Delta I}$ in Engbers et al. (2022a). (A) *PSVM* spatial distribution of localities in *PSVM*, $PSVM_N$ and $PSVM_R$. Numbers correspond to the localities listed in Supp. Table S1. Boxes C and J are enlargements of the Canary Islands and Japan, respectively. Green localities are present in the Normal, Reverse and Combined dataset; Magenta localities are present in the Reverse and Combined dataset; Blue localities are present in the Normal and Combined dataset; and yellow localities are only present in the Combined dataset. Localities are left out if $N < 10$, after the Vandamme cut-off (Vandamme, 1994). *PSVM* is described in detail in Supplementary Information S1. (B) Histogram of the temporal distribution of the sites in *PSVM*, $PSVM_N$ and $PSVM_R$.

Table 1
PSVM (*PSVM*$^{\Delta I}$ in Engbers et al. (2022a)), the dataset used for our complete MTAM1 model. For the normal (*PSVM*$_N$) and reverse (*PSVM*$_R$) dataset the locality averages were recalculated using only the normal or only the reverse sites for each locality, respectively. Locality_ID is the number that coincides with the numbers in Fig. 1 of the main text, and with the localities in Engbers et al. (2022a). Localities 3, 8, 13, 39 and 41–42 from *PSVM* were excluded for *PSVM*$^{\Delta I}$, as they experienced local vertical axis block rotations. N is the number of sites in the locality after the Vandamme cutoff was applied (Vandamme, 1994). Age (Ma) is the average age per locality. Lat and Long are the sample latitude and longitude after plate reconstructions described in Section S1 above. VGPlat and VGPlong are the latitude and longitude of the virtual geomagnetic pole of that locality, calculated with the rotated declination and inclination and with the location corrected for plate movement. Dec and Inc are the declination and inclination for that locality in degrees, rotated and corrected for plate movement as described in Section S1. Dec Old is the original Declination calculated for each locality, without considering the rotation of the plates (as presented in Engbers et al. (2022a). ΔI is the inclination anomaly with respect to GAD (ΔI $= I - I_{GAD}$), which together with Dec forms the misfit from GAD in this locality. Location is the country where the samples were originally sampled. More information about this data can be found in Engbers et al. (2022a), and the individual site date can be found in Supplementary Material Dataset S1.

Locality_ID	N	Age (Ma)	Lat	Long	VGPLat	VGPLong	Plat	Dec	Inc	A_{95}	Dec Old	ΔI	Location
1	52	12.5	63.32	344.10	117.81	344.85	86.55	4.91	73.28	4.5	7.07	1.50	Iceland
2	19	6.1	64.12	343.93	20.34	344.37	80.94	15.26	79.38	4.8	16.20	−3.81	Iceland
3							*Excluded*						*Canada*
4	31	16.5	48.16	5.00	−105.17	6.29	83.44	351.53	62.47	5.8	355.71	2.71	Germany
5	27	5.6	45.91	24.05	−104.50	22.93	85.91	355.58	61.47	5.7	6.92	2.08	Romania
6	82	13.3	47.98	245.29	20.36	250.85	81.44	8.78	60.27	3.2	2.25	4.74	USA
7	12	9.5	43.69	2.13	169.57	2.90	66.11	5.67	34.48	31.9	8.03	26.77	France
8							*Excluded*						*USA*
9	20	12.0	43.19	114.55	−24.53	116.26	80.86	352.70	57.18	3.1	355.55	6.8	China
10	29	18.0	41.59	107.94	−115.40	110.39	79.86	9.02	55.87	6.0	13.44	6.64	China
11	10	14.0	40.93	138.16	−152.77	139.36	80.05	13.48	64.73	7.7	9.31	−2.38	Japan
12	11	16.0	40.23	137.29	−61.95	138.43	81.67	3.55	54.86	8.2	358.97	7.15	Japan
13							*Excluded*						*Greece*
14	18	8.3	38.23	248.31	83.55	252.40	85.29	358.92	52.13	10.7	354.08	3.86	USA
15	29	10.0	38.48	137.35	−71.64	139.37	79.61	6.23	50.33	6.4	7.00	8.99	Japan
16	13	13.5	37.02	128.72	−21.79	132.07	84.11	356.88	53.24	10.4	358.53	5.17	Japan
17	32	15.3	37.15	133.23	−74.70	137.28	77.81	7.34	47.82	7.4	8.70	10.91	Japan
18	154	16.1	35.55	248.93	62.25	254.52	84.95	1.23	48.29	2.3	354.89	5.40	USA
19	28	9.3	27.53	344.95	−152.18	346.51	86.12	357.22	40.13	5.7	356.99	3.93	Lanzarote
20	24	5.7	27.46	342.26	128.06	343.31	84.25	3.56	37.95	5.6	3.18	6.38	Tenerife
21	54	9.7	26.64	341.34	−77.93	343.02	80.96	350.97	47.85	8.0	350.51	−5.11	La Gomera
22	86	14.1	25.76	342.03	165.55	344.55	76.15	359.76	18.95	9.0	359.03	22.19	Gran Canaria
23	30	13.8	27.55	249.69	164.38	258.39	82.51	351.85	41.08	4.9	353.36	1.02	Mexico
24	11	9.4	21.49	258.17	28.54	261.01	87.41	2.17	34.32	10.3	358.48	2.37	Mexico
25	37	10.8	21.43	258.26	120.35	261.47	84.33	356.30	29.48	3.3	352.21	6.94	Mexico
26	10	8.5	20.54	262.85	−114.28	265.38	85.15	358.22	41.75	15.4	354.85	−6.42	Mexico
27	22	20.7	19.96	263.07	−151.59	268.95	84.42	354.82	36.50	8.7	348.10	−4.06	Mexico
28	34	15.5	13.64	264.64	93.32	270.36	84.72	359.73	15.26	6.2	352.51	8.32	Honduras
29	32	13.0	7.43	36.82	−113.04	39.30	86.03	358.15	7.08	6.2	1.21	6.86	Ethiopia
30	17	21.0	0.90	5.37	−19.11	9.81	86.37	358.24	4.45	9.9	359.66	−6.35	Cameroon
31	21	15.4	1.94	6.80	−106.23	10.03	83.14	353.85	−5.29	12.2	355.16	6.06	Cameroon
32	10	9.1	2.27	7.56	147.74	9.45	79.03	7.33	−14.10	31.1	8.37	16.12	Cameroon
33	38	7.0	−1.02	5.11	−99.75	6.63	87.16	357.27	−6.07	4.3	357.99	1.58	São Tomé
34	12	10.0	−4.84	327.97	−173.06	330.55	87.44	358.46	−17.35	11.6	358.94	3.91	Fernando de Noronha
35	20	20.0	−15.85	286.12	−141.80	291.30	85.89	355.86	−33.19	7.6	353.79	−1.9	Peru
36	37	9.4	−17.55	352.00	−18.76	354.37	82.42	358.25	−22.66	7.8	358.50	−12.16	Saint Helena
37	13	9.0	−23.14	293.19	−47.15	295.18	81.53	2.68	−31.23	7.0	1.31	−11.73	Argentina
38	13	16.0	−41.12	142.64	45.36	147.34	88.58	358.22	−57.94	7.3	5.96	−2.03	Australia
39							*Excluded*						*Chile*
40	21	10.6	−46.26	177.40	−145.02	179.21	87.96	1.62	−61.41	6.0	358.25	−1.38	New Zealand
41							*Excluded*						*New Zealand*
42							*Excluded*						*New Zealand*
43	14	12.0	−48.80	175.65	−29.52	177.73	85.66	3.11	−67.40	12.1	359.18	2.86	New Zealand
44	27	21.0	−49.04	67.23	72.41	74.95	83.67	359.62	−60.86	5.6	6.27	−5.06	Kerguelen Islands

et al., 2018)) or with separate models for the normal and reversed fields (e.g. LN1 and LR1 (Johnson and Constable, 1995)). If we could combine the normal and reverse fields to create the time-averaged field models, the resolution of such models would increase greatly.

In this study, we test the hypothesis of a polarity symmetry in the TAF by creating and comparing the first TAF models for the Miocene. We begin by generating normal and reverse models *MTAM1*$_N$ and *MTAM1*$_R$ using the data separated by polarity from *PSVM*$_N$ and *PSVM*$_R$. We further analyse a combined data set, assuming equivalence with the sign of *PSVM*$_R$ reversed, generating a combined model designated MTAM1. This data set provides the best coverage in space and time and hence, if the unification can be justified, the best-resolved combined model MTAM1. These models will be used to investigate the morphology of the geomagnetic field in the Miocene, possible polarity asymmetry in that morphology, and whether recurring irregular features in the South Atlantic are sufficiently frequent and coherent to appear in the morphology of the field when averaged over long periods of time.

2. Theory

The geomagnetic field of the Earth can be expressed as the gradient of the potential (Ψ):

$$B = -\nabla\Psi. \tag{1}$$

conveniently expanded in a series of spherical harmonics:

$$\Psi\ (r,\theta,\varphi) = a\sum_{l=1}^{\infty}\sum_{m=0}^{l}\left(\frac{a}{r}\right)^{l+1} \times \left(g_l^m \cos m\varphi + h_l^m \sin m\varphi\right) P_l^m(\cos\theta) \tag{2}$$

Here r, is the distance from the Earth's centre, a is the Earth's radius, θ and φ are the colatitude and longitude. P_l^m are the semi-normalised Schmidt functions and g_l^m and h_l^m Gauss coefficients, the values of

which define the field morphology (Holme and Bloxham, 1996). The vector components of the magnetic field are then

$$B_r = -\frac{\partial \Psi}{\partial r},\ B_\theta = -\frac{1}{r}\frac{\partial \Psi}{\partial \theta},\ B_\varphi = -\frac{1}{r\sin\theta}\frac{\partial \Psi}{\partial \varphi} \tag{3}$$

The vector components depend linearly on the spherical harmonic coefficients, and so these coefficients can be obtained by linear inversion, but palaeomagnetic data are measured as declination and inclination, which are given by the equations:

$$D = \tan^{-1}\left(\frac{B_\varphi}{-B_\theta}\right),\ I = \tan^{-1}\left(\frac{-B_r}{\left(B_\theta^2 + B_\varphi^2\right)^{\frac{1}{2}}}\right) \tag{4}$$

These observations depend non-linearly on the coefficients, so their inversion is also non-linear, and requires iterative solution. We seek the set of spherical harmonic coefficients that leads to a good fit to the observed measurements of declination and inclination, but avoiding excessive model complexity. Formally, there are an infinite number of such coefficients; we therefore truncate the series to a defined spherical harmonic degree l. We define a vector of the available data $\boldsymbol{\gamma}$,which obeys the equation $\boldsymbol{\gamma} = \boldsymbol{f}(\boldsymbol{m}) + \boldsymbol{e}$, where $\boldsymbol{f}(\boldsymbol{m})$ is the non-linear function that predicts the observations from the spherical harmonic coefficients, and the misfit defined by the error vector $\boldsymbol{e}$. We seek the model vector $\boldsymbol{m}$ which minimises the residual

$$\boldsymbol{e}^T \boldsymbol{C}_e^{-1} \boldsymbol{e}, \tag{5}$$

$\boldsymbol{C_e}$ is the diagonal data covariance matrix for the errors (assuming that the errors are uncorrelated). The α_{95} for the site mean is used as the inclination error in this matrix. For the declination error we divide the α_{95} by the cosine of the inclination in radians. As there are an infinite number of Gauss coefficients to solve for, and limited and unevenly distributed data, an additional smoothing constraint was added, with strength controlled by a damping parameter. The spherical harmonics are truncated at degree $L = 14$ yielding $L(L+2) = 224$ coefficients, a sufficiently high resolution that the small-scale structure is controlled by damping and is therefore insensitive to the precise truncation degree. The level of truncation therefore does not determine the level of resolution of these models, the damping does this instead. We minimize the objective function $\boldsymbol{\Phi}(\boldsymbol{m})$ in Eq. (6):

$$\boldsymbol{\Phi}(\boldsymbol{m}) = (\boldsymbol{\gamma} - \boldsymbol{f}(\boldsymbol{m}))^T \boldsymbol{C}_e^{-1} (\boldsymbol{\gamma} - \boldsymbol{f}(\boldsymbol{m})) + \lambda \boldsymbol{m}^T \boldsymbol{C}_m^{-1} \boldsymbol{m}, \tag{6}$$

where the Lagrange multiplier, λ, is a damping parameter controlling the weight applied by $\boldsymbol{C}_m^{-1}$, a positive definite matrix based on the norm function. This norm function can be based on many forms of damping, but in our models it is based on the minimisation of the squared radial field intensity integrated over the CMB (Holme and Bloxham, 1996). The model optimization is now dependent on a minimum misfit $\boldsymbol{e}^T \boldsymbol{C}_e^{-1} \boldsymbol{e}$, and a minimum norm, $\lambda \boldsymbol{m}^T \boldsymbol{C}_m^{-1} \boldsymbol{m}$. The model is iterated to find a minimum of $\boldsymbol{\Phi}(\boldsymbol{m})$ for each different damping parameter which is done with the iteration in Eq. (7), depending on the matrix of Fréchet derivatives $\boldsymbol{A}$.

$$\boldsymbol{m}_{i+1} = \boldsymbol{m}_i + \left(\boldsymbol{A}^T \boldsymbol{C}_e^{-1} \boldsymbol{A} + \boldsymbol{C}_m^{-1}\right)^{-1} \left(\boldsymbol{A}^T \boldsymbol{C}_e^{-1} (\boldsymbol{\gamma} - \boldsymbol{f}(\boldsymbol{m}_i)) - \boldsymbol{C}_m^{-1} \boldsymbol{m}_i\right),\ \boldsymbol{A} = \left.\frac{\partial \boldsymbol{f}(\boldsymbol{m})}{\partial \boldsymbol{m}}\right|_{\boldsymbol{m}=\boldsymbol{m}_i} \tag{7}$$

This iteration ends when $\boldsymbol{\Phi}(\boldsymbol{m}_n) - \boldsymbol{\Phi}(\boldsymbol{m}_{n-1})$ is at a minimum, which in theory is when $\boldsymbol{\Phi}(\boldsymbol{m}_n) - \boldsymbol{\Phi}(\boldsymbol{m}_{n-1}) \ll 1$. In practice the iteration ends when $\boldsymbol{\Phi}(\boldsymbol{m}_n) - \boldsymbol{\Phi}(\boldsymbol{m}_{n-1})$ is no longer making significant changes to $\boldsymbol{m}$ (Gubbins and Bloxham, 1985; Panovska et al., 2015).

Optimal models are determined for a range of damping parameters. Varying λ leads to a trade-off between the normalised roughness and the misfit (Gubbins and Bloxham, 1985; Holme and Bloxham, 1996). The Lagrange multiplier, or damping parameter is varied between strongly damped (large λ) towards the prior model (the original estimate of the field where we start our iterations, usually GAD), to allowing a model which is overly sensitive to the data (small λ). To obtain the preferred value for λ, we consider the trade-off between misfit and complexity; we seek a model that provides good fit to data without requiring excessive complexity.

The average data vector, $\boldsymbol{\gamma}$, consists of the average inclinations and declinations for the data-groups in *PSVM* (and $PSVM_N$ and $PSVM_R$) (Engbers et al., 2022a); these were determined using the Vandamme cut-off (Vandamme, 1994). As the models are based on directional data only (PSVM), and not on full-vector data, the Gauss coefficients in the resulting model are nonunique in magnitude, and can be scaled by free choice of the coefficient g_1^0, the axial dipole.

First the separate datasets, $PSVM_N$ and $PSVM_R$, were modelled with GAD as a default prior and starting model. We therefore, avoid bias from our choice of starting model, by choosing the model of minimal complexity – the axial dipole. Applying a Bayesian interpretation, we can consider the likelihood of certain features of the field being required by the data, but with the model results biased towards the existing beliefs regarding the field, specifically that the field is of minimum magnitude. Those features present for high values of λ are those most strongly required by the data.

3. Inversion results

3.1. Results for $PSVM_N$ and $PSVM_R$

To determine the best balance between the data fit and constraint for the model, a trade-off curve plotted of the normalised roughness value against the misfit is used as a guide to a preferred model. Ideally, the preferred model is that where the trade-off curve shows a “knee”, for which the misfit is minimised without the roughness of the model increasing too far. While (like many inverse problems) here the knee is not sharp, we choose a value providing a suitable compromise between misfit and complexity (Supplementary Material Fig. S1). For the normal dataset, $PSVM_N$, the result of the optimal damping parameter, chosen so as to observe the robust features of the field but restrict the non-robust features is called $MTAM1_N$, for the normalised $PSVM_R$ dataset, the same process was used as for $PSVM_N$ (Supplementary Material Fig. S2). Fig. 2 shows $MTAM1_R$ and $MTAM1_N$ together with the different data localities. The models are sufficiently similar that the differences may arise from differences in data distribution. The main difference is the form of the northern high latitude flux lobe over Canada with an RFP west of that in $MTAM1_N$. They both include the RFP under Western Africa, and similar (yet not identical) features under Central America and South-East Asia. This suggests that the fields might be close to symmetrical, especially considering that the differences may result from inconsistent data distribution between the two models, which are also shown in Fig. 2. To test this hypothesis, new models were created with $PSVM_N$ and $PSVM_R$ and the model with opposite polarity as a prior instead of a GAD prior. The differences between the resulting models ($MTAM1_N$' and $MTAM1_R$', Supplementary Material Fig. S3) are even smaller, suggesting that the differences may be explained by the different spatial sampling of the datasets. This polarity-symmetric field suggests the possibility of combining the normal and reverse dataset to look at the average morphology of the field for the entire Miocene, instead of the normal and reverse chrons separately.

3.2. Results for combined dataset, PSVM

When the entirety of *PSVM* can be used for the non-linear inverse problem, the dataset increases from 26 (20) localities for the normal (reverse) dataset to 38 localities in the complete dataset (PSVM). The improved data distribution strengthens the model, allowing more detail to be seen in the field morphology. Fig. 3 shows the optimal model MTAM1 based on PSVM, which was created using the same techniques

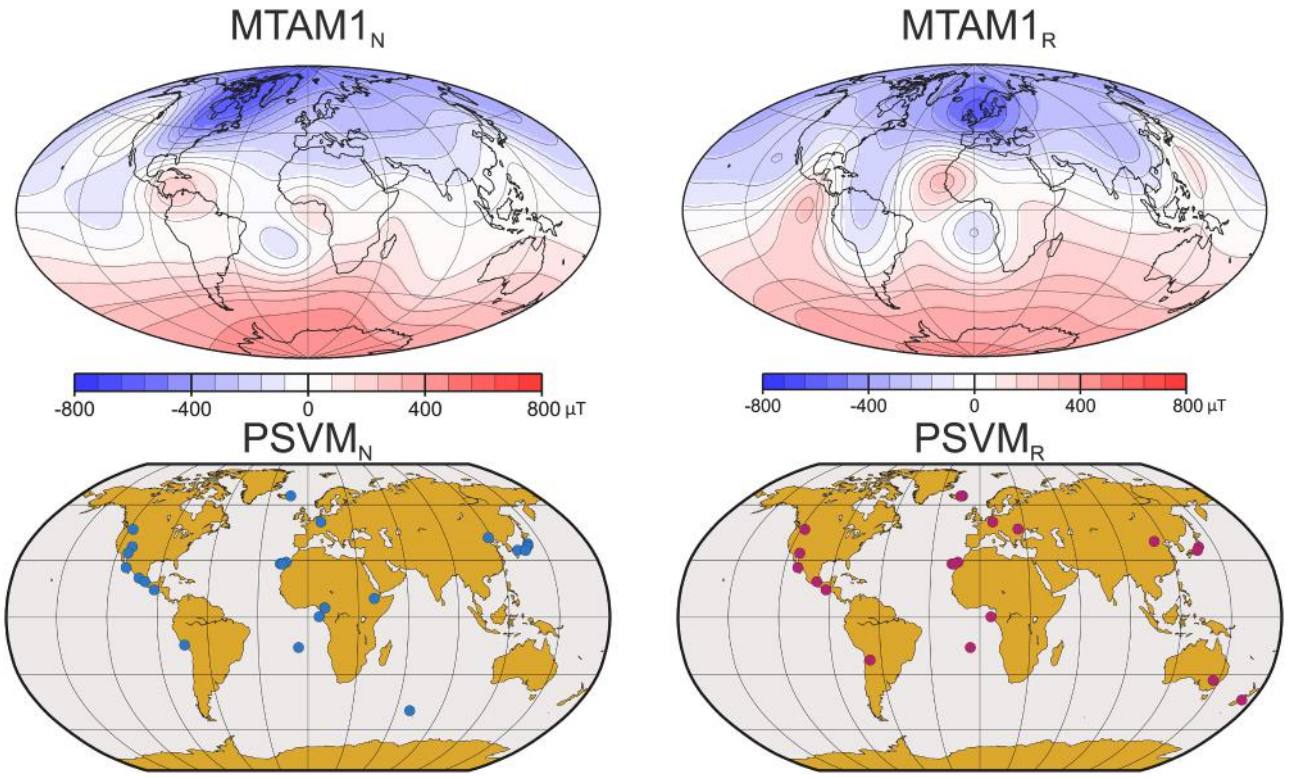

Fig. 2. (Top) Radial field (B_r) on the CMB in μT for $MTAM1_N$ (left) and $MTAM1_R$ (right). (Bottom) The data locations for $PSVM_N$ in blue (left) and $PSVM_R$ in pink (right). It's important to note that due to the Green's functions that control downwards continuation, the effect of the data points at the surface is not directly affecting the same location at the CMB (Johnson & McFadden, 2015).

as the $MTAM1_N$ and $MTAM1_R$ models (Supplementary Material Fig. S4). The radial field model for MTAM1 shows that the RFPs under Central to South America and under western Africa to South Atlantic are both sufficiently stable to appear in the TAF model. MTAM1 is our preferred model of the Miocene TAF. The Gauss Coefficients for MTAM1, $MTAM1_N$ and $MTAM1_R$ are available in the supplementary material. These do not represent the true field but give a non-unique solution for the TAF in the Miocene. Fig. 4 shows the power spectra for MTAM1, $MTAM1_N$ and $MTAM1_R$, showing again that the results do not differ substantially between models.

4. Discussion

4.1. Validity/robustness of the results

As for all non-unique inverse problems, the results are only a possible solution, and should be used to test for certain features in the field and not taken as the true morphology of the TAF at that time. The results suggest certain features are needed to achieve an adequate fit to data even with different prior models, and with either the normal or reverse datasets. The data quality is high (Engbers et al., 2022a); however, spurious data are still possible, and in optimisation problems such as these, outliers can strongly influence the model. Supplementary Material Fig. S5 shows the declination and inclination points for MTAM1, the data and the misfit between data and model. It is clear that outliers are present, especially in the high latitudes, but that the model did not form a local optimum based on those outliers. The inclination is particularly well fit, whereas the declination is shown to be less coherent. The models seem to have been focused on the more robust datapoints in the lower latitude range. The common features that are shown in MTAM1, $MTAM1_N$ and $MTAM1_R$, suggest that the *PSVM* dataset is sufficiently large and well distributed to create meaningful non-zonal TAF models for the Miocene. Some of the outliers are also averaged out with nearby localities, like in the case of Gran Canaria, where the high inclination anomaly (22.19°) is averaged out by the results from Lanzarote, Tenerife and La Gomera. The code averages such data in any case making any combination into a single data point unnecessary. Supplementary Fig. S6 shows the MTAM1 model when combining the localities from the Canary Islands as one locality, and the localities from New Zealand as one locality. It shows that this does not affect the results. One specific outlier in the inclination anomaly is around 43° latitude, which represents locality #7, France. This inclination anomaly is 26.77° and is not averaged out by other data. Supplementary Fig. S5 shows that the model does not form around this outlier, and when running the model without this datapoint (Supplementary Fig. S7) the results are hardly affected.

4.2. Symmetry of the magnetic field

The dipole only makes up 39% of the power of the geomagnetic field at the CMB compared to 93% at the surface (Alken et al., 2021). The reversal of the dipole therefore does not automatically mean the entire field reverses. Previous TAF models have been based on normal or reverse data separately (e.g. LN1 and LR1, (Johnson and Constable, 1997)). As the differences between the $MTAM1_N$ and $MTAM1_R$ morphology are small, and even more so between the results for the normal dataset with $MTAM1_R$ as prior and vice-versa, our results provide no evidence that the geomagnetic field in the Miocene behaved differently during its normal and reverse states. We therefore cannot reject the hypothesis that the field is completely reversible and that there are no substantial parts of the field that are independent of the polarity of the dipole. Nevertheless, heterogeneity within the lowermost mantle could still lead to persistent nondipolar components in the geomagnetic field that are prone to reversing together with the dipole. These findings suggest normal and reverse paleomagnetic data can be combined for TAF models, increasing the resolution of these models substantially.

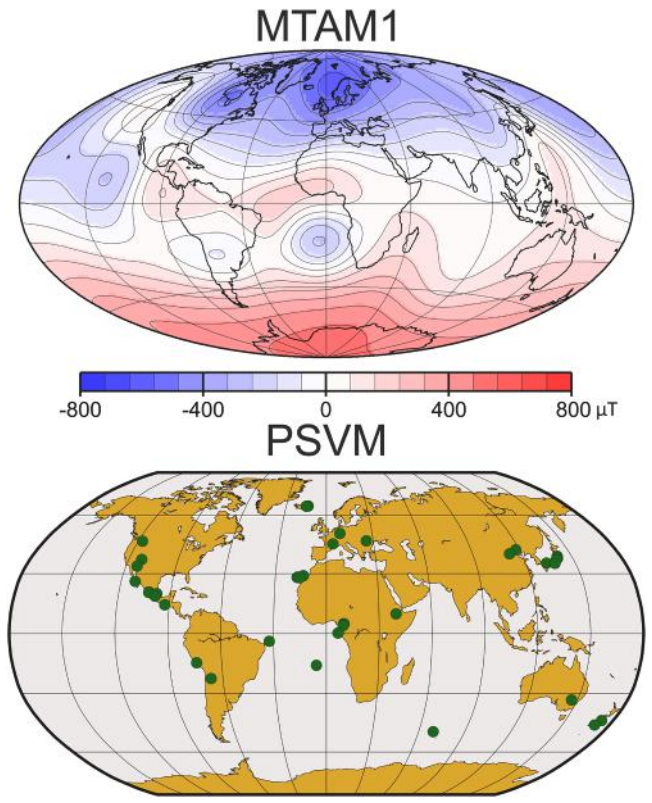

Fig. 3. (Top) Radial field, B_r, in μT on the CMB for MTAM1, the preferred TAF model for the combined *PSVM* dataset. (Bottom) The *PSVM* dataset location in green. It's important to note that due to the greens functions that control downwards continuation, the effect of the data points at the surface is not directly affecting the same location at the CMB (Johnson & McFadden, 2015).

4.3. South Atlantic reverse flux patch

The observation of the persistent RFP under the South Atlantic and western Africa is of particular significance as it has been suggested that its presence is related to lowermost mantle heterogeneity and specifically to the Large Low Shear Velocity Province (LLSVP) seen in seismological models of the deep mantle under Africa (Shephard et al., 2017; Tarduno et al., 2015). Our results, no matter which prior or which dataset (normal, reverse or combined) all show that an RFP in this location is strongly indicated by the data. When the damping parameter of MTAM1 (Fig. 5), is decreased from an initial choice of a high damping that you get an approximation of GAD, the first structure that appears is the RFP in the South Atlantic. This suggests that this RFP is a necessary feature to satisfy the data, and that stepping away from this feature would be to reduce the impact of coherent signal in data to let the model be dominated by its prior. This builds on our confidence that an RFP in the South Atlantic is required by the data in PSVM. This RFP in MTAM1 agrees with the finding of Engbers et al. (2020, 2022a) and Tarduno et al. (2015) that the SAA is not a singular event and that this region has been experiencing irregular behaviour on a multi-million-year timescale. It further suggests that the RFP reoccurs so frequently and persists for so long that it is not averaged out over a substantial amount of time in the TAF on the CMB. To test the dependence on the one datapoint from Saint Helena we ran the model with the *PSVM* dataset with Saint Helena excluded. This also showed a similar RFP under Africa as in MTAM1 (Supplementary Fig. S8), suggesting that this result is not critically dependent on the data from Saint Helena where the SAA was shown to be a long-lasting feature (Engbers et al., 2020, 2022b). This feature is not sufficiently strong to produce a strong surface SAA in the averaged field, as shown in the Supplementary Fig. S9. Notwithstanding differences in data availability between them (Fig. 1), the model structure suggests a difference in robust features between the Atlantic and Pacific hemispheres. The heterogeneity at the CMB in the Atlantic Hemisphere is substantially stronger than in the Pacific Hemisphere. This is in line with many previously performed studies in PSV, numerical simulation and non-zonal TAF models on all scales (Aubert et al., 2013; Brown et al., 2018; Holme et al., 2011; Jackson et al., 2000; Korte and

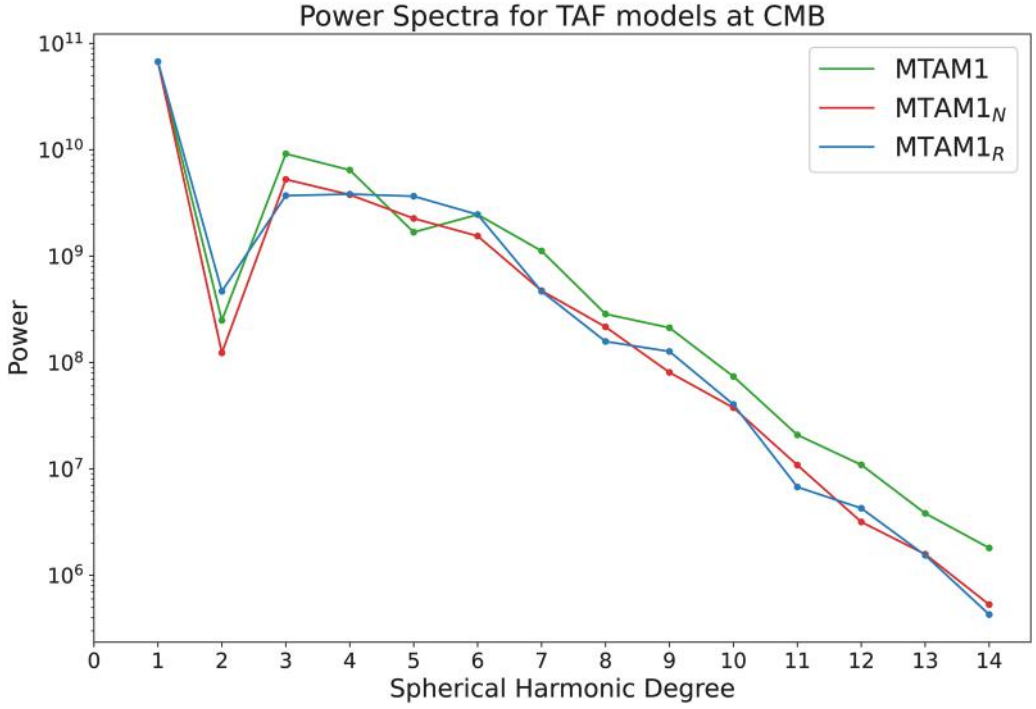

Fig. 4. The power spectra for MTAM1 (green), *MTAM1*$_N$ (red) and *MTAM1*$_R$ (blue) at the CMB.

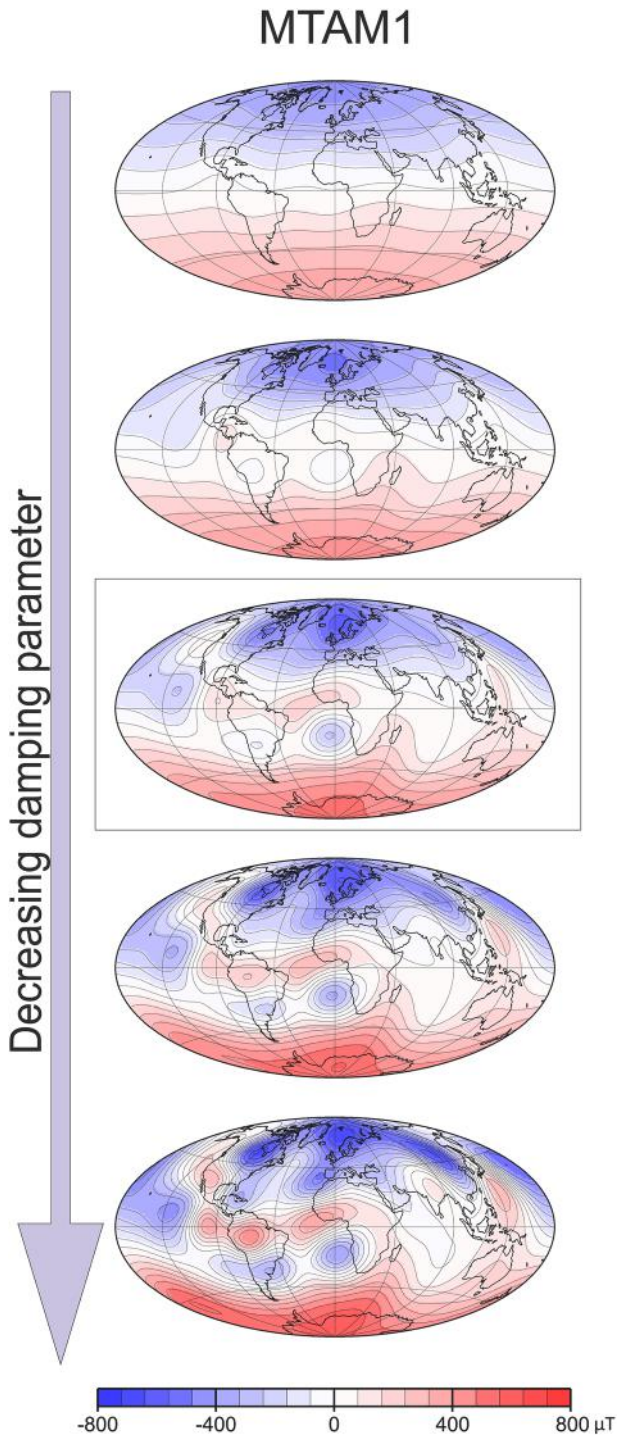

Fig. 5. Five versions of MTAM1 with a varying damping parameter. The damping parameter decreases from a very high damping parameter and thus an approximation of GAD (top) to very low damping parameter and thus over-representation of the data (bottom). The middle model in the grey box is our preferred model.

Constable, 2003; Panovska et al., 2019; Ziegler and Constable, 2015).

4.4. Comparison between Miocene and the past 5Myr

At first sight, $MTAM1_N$ shows some important differences in structure to LN3 from Cromwell et al. (2018) (Fig. 5). Most compelling are the RFPs under the South American and South Atlantic regions. Some of the nondipolar features in LN3 do show up in the same locations in $MTAM1_N$. West Africa and Central to South America are where the morphology of the field shows its non-GAD features in both models. The differences between both models may be due to a difference in damping parameter. To test the effect of varying the damping parameter, LN3 was recreated using the same PSV10 dataset for the past 5 Myr and only the normal polarity data, as for the original LN3. The only difference from the original study is that the data from PSV10 were divided into the localities of Sprain et al. (2019) instead of 5° to 10° geographical bins as done for LN3. We were able to recreate LN3 with our version of the PSV10 localities without seeing substantial deviations (Supplementary Fig. S10). LN3' as shown in Fig. 5, has a similar level of detail to $MTAM1_N$. Aside from the large RFP in the Pacific in LN3' and the lack of the RFP in the Atlantic, the two models are very similar, especially at low latitudes. The two differences are easily explained by the presence of data from Hawaii uniquely in model LN3' and from Saint Helena in model $MTAM1_N$. The similarities between the models, and specifically the similarities in location of features around central America, Africa, the Indian Ocean and Australia, suggest that such features are robust. This strengthens the argument for long lasting effects of CMB heat flux heterogeneity on the magnetic field morphology.

The smoothness constraint chosen for LN3 by Cromwell et al. (2018) is based on minimum non-GAD structure, leaving very little morphology to be interpreted. We argue that this conservative method has left LN3 to miss certain features in the TAF structure that appear to be robust over time. One of the features that was undeniably present in the MTAM1 models was the RFP under Africa. Although some non-GAD morphology is present, and a large undulation in the magnetic equator is present in the Atlantic, this RFP is not present in LN3'. This might be due to the lack of data in the South Atlantic in PSV10 for 0–5 Myr. To check this, $MTAM1_N$ was used as a prior for LN3', to create a new model called LN3'' (Fig. 6). Only the Pacific RFP requires a strong deviation from $MTAM1_N$. Fig. 7 shows that LN3' and LN3'' ($MTAM1_N$ prior) have a similar misfit, indicating that the data from the last 5 Myr do not require a model with strong differences from the Miocene model. The additional complexity (increased roughness) in the LN3' morphology, arises from model complexity required by fitting $MTAM1_N$ in regions where LN3 data are lacking. This suggests that the geomagnetic field has been stable with consistent, distinctive features in the morphology for at least the past 23 Myr. This is expected if departures from GAD arise from core-mantle coupling (thermal, electromagnetic, topographic or gravitational) and thus from long-lasting mantle control on the geomagnetic field structure because we would expect little change in lower mantle structure on such timescales (Hager, 1984; Torsvik et al., 2010).

Our conclusions depend at least in part on our choice of a closer fit to data than adopted for other models (in particular the original LN3). On one level, this reflects a (small) difference in philosophy – we choose to place greater confidence in the information provided by the data relative to the prior assumptions. While our choice might be regarded by some as overoptimistic, we feel strongly supported by the coherence between the models for the past 5 Million years and our models for the Miocene. We encourage future modellers to also investigate closer fits (and so higher resolution models); only by doing so will we utilise the information provided by the data to its fullest.

5. Conclusions

The MTAM1 model, together with $MTAM1_N$ and $MTAM1_R$ for the normal and reverse datasets respectively, have shown us that the PVSM dataset is of sufficient size and distribution to create useful non-zonal TAF models through spherical harmonics. The relatively similar results for $MTAM1_N$ and $MTAM1_R$ and even more similar results for their respective models with the other as a prior show us that the field in the Miocene was on average, close to symmetric. This suggests that the entire field reverses during a transition or reversal, and that the normal and reverse data can be taken together when normalized to create a complete TAF model with a higher resolution. The robust feature of the

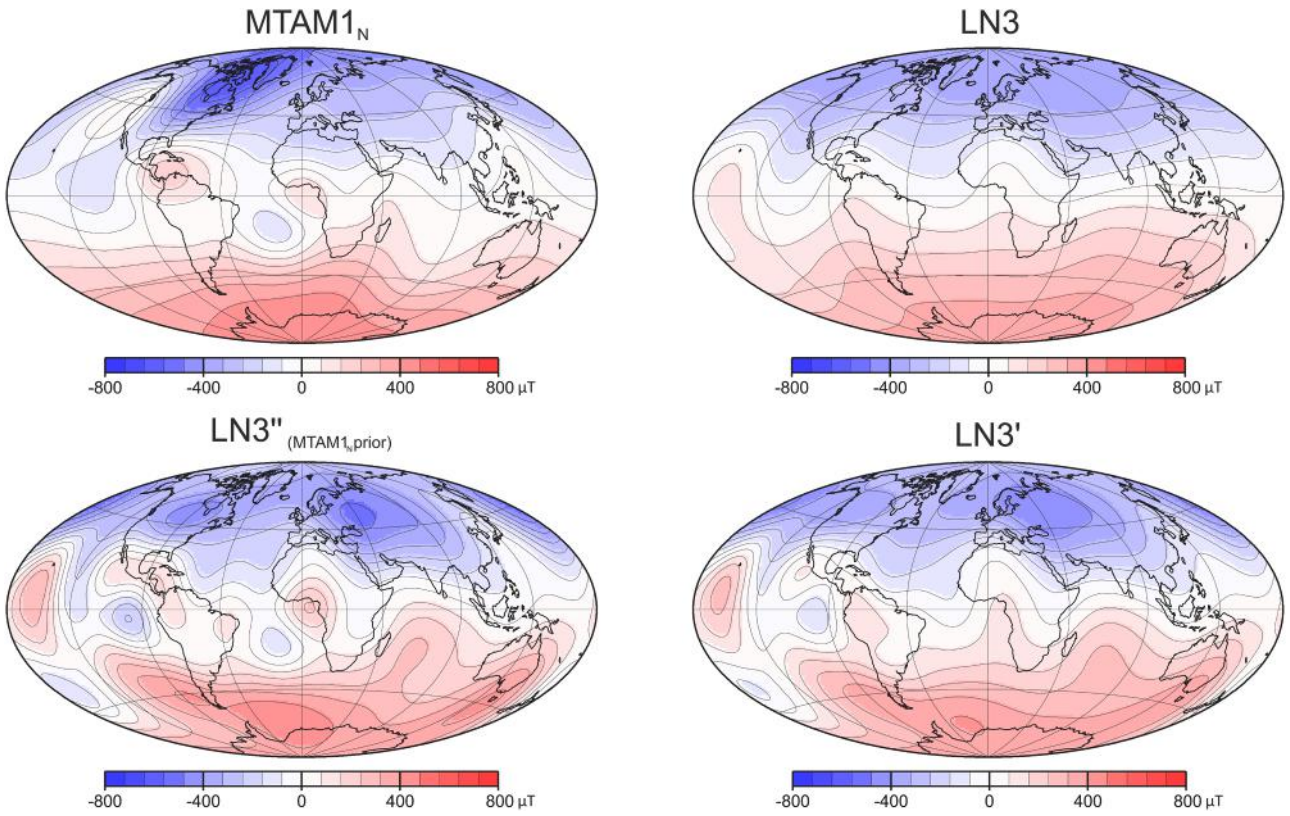

Fig. 6. The radial field, Br, at the CMB in μT for *MTAM1$_N$* (top left) and LN3 (Cromwell et al., 2018) (top right). LN3' (bottom right) and LN3'' (bottom left). LN3' is a new version of LN3, created with the same dataset (PSV10$_N$, 0–5 Myr) but divided in different localities and with less damping, making the comparison with *MTAM1$_N$* more valid. LN3'' is a new version of LN3 with the same dataset (PSV10$_N$, 0–5 Myr) but divided in different localities and with less damping, and *MTAM1$_N$* as a prior.

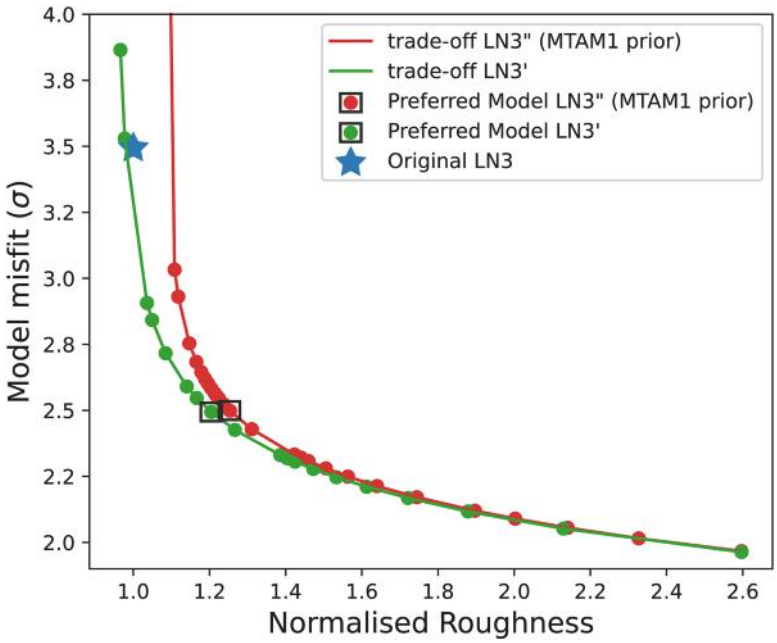

Fig. 7. The trade-off curve between the misfit and the normalised roughness for LN3' in green and LN3'' (*MTAM1$_N$* prior) in red. The black squares on the green and red curve denote the preferred models shown in Fig. 5 and Fig. 6, respectively. The blue star represents the norm and misfit for the original LN3 model by Cromwell et al. (2018).

South American RFP in our models show that the anomalous behaviour in that region has been sufficiently frequent and spatially stable enough in the Miocene to not be averaged out by the TAF. Although there is limited data in the Southern Hemisphere to represent this feature, we have shown that the feature is not dependent on the dataset from Saint Helena. The location of the RFP under South America and western Africa brings further evidence of a link between the African LLSVP and this RFP. The lack of significant differences between the TAF for the Miocene

and that of the past 5 Myr, suggests that the geomagnetic field has been experiencing consistent features and deviations from GAD for at least the past 23 Myr, which is expected when assuming long-lasting mantle control on the geomagnetic field structure (Mound and Davies, 2023).

CRediT authorship contribution statement

Y.A. Engbers: Writing – original draft, Methodology, Investigation, Formal analysis, Data curation. **R. Holme:** Writing – review & editing, Visualization, Supervision, Software, Methodology, Conceptualization. **A.J. Biggin:** Writing – review & editing, Supervision, Project administration, Funding acquisition, Conceptualization.

Declaration of Competing Interest

The authors declare that they have no known competing financial interests or personal relationships that could have appeared to influence the work reported in this paper.

Data availability

The data is available in the Supplementary Material.

Acknowledgments

This work was supported by The Leverhulme Trust (RL-2016-80) and NERC grant NE/T012463/1. The datasets used for the models have previously been published as a dataset and as individual data papers which are all given in the complete dataset (dataset S1: *PSVM*) in the supplementary material. The Gauss Coefficients of MTAM1, $MTAM1_N$ and $MTAM1_R$ have been included in the supplementary material as GG-C, GG-N and GG-R.

Supplementary materials

Supplementary material associated with this article can be found, in the online version, at doi:10.1016/j.epsl.2023.118535.

References

Alken, P., Thébault, E., Beggan, C.D., Amit, H., Aubert, J., Baerenzung, J., et al., 2021. International geomagnetic reference field: the thirteenth generation. Earth Planets Space 73 (1). https://doi.org/10.1186/s40623-020-01288-x.

Aubert, J., Finlay, C.C., Fournier, A., 2013. Bottom-up control of geomagnetic secular variation by the Earth's inner core. Nature 502 (7470), 219–223. https://doi.org/10.1038/nature12574.

Brown, M., Korte, M., Holme, R., Wardinski, I., Gunnarson, S., 2018. Earth's magnetic field is probably not reversing. Proc. Natl. Acad. Sci. U. S. A. 115 (20), 5111–5116. https://doi.org/10.1073/pnas.1722110115.

Constable, C.G., Korte, M., Panovska, S., 2016. Persistent high paleosecular variation activity in southern hemisphere for at least 10 000 years. Earth Planet. Sci. Lett. 453, 78–86. https://doi.org/10.1016/j.epsl.2016.08.015.

Cromwell, G., Johnson, C.L., Tauxe, L., Constable, C.G., Jarboe, N.A., 2018. PSV10: a global data set for 0–10 Ma time-averaged field and paleosecular variation studies. Geochem. Geophys. Geosyst. 19 (5), 1533–1558. https://doi.org/10.1002/2017GC007318.

Engbers, Y.A., Bono, R.K., Biggin, A.J., 2022a. PSVM: a global database for the Miocene indicating elevated paleosecular variation relative to the last 10 Myrs. Geochem. Geophys. Geosyst. 23 (8), 1–16. https://doi.org/10.1029/2022GC010480.

Engbers, YA., Biggin, A.J., Bono, R.K., 2020. Elevated paleomagnetic dispersion at Saint Helena suggests long-lived anomalous behavior in the South Atlantic. Proc. Natl. Acad. Sci. U. S. A. 117 (31), 18258–18263. https://doi.org/10.1073/pnas.2001217117.

Engbers, YA., Grappone, J.M., Mark, D.F., Biggin, A.J., 2022b. Low paleointensities and Ar/Ar ages from Saint Helena provide evidence for recurring magnetic field weaknesses in the South Atlantic. J. Geophys. Res. Solid Earth 1–14. https://doi.org/10.1029/2021jb023358.

Evans, D.A.D., 2006. Proterozoic low orbital obliquity and axial-dipolar geomagnetic field from evaporite palaeolatitudes. Nature 444 (7115), 51–55. https://doi.org/10.1038/nature05203.

Gubbins, D., Bloxham, J., 1985. Geomagnetic field analyses - III. magentic fields on the core-mantle boundary. Geophys. J. R. Astron. Soc. 80, 695–713.

Hager, B.H., 1984. Constraints on mantle rheology and flow residual geoid: degree 2-10. J. Geophys. Res. 89 (4), 6003–6015.

Holme, R., Olsen, N., Bairstow, F.L., 2011. Mapping geomagnetic secular variation at the core-mantle boundary. Geophys. J. Int. 186 (2), 521–528. https://doi.org/10.1111/j.1365-246X.2011.05066.x.

Holme, R., Bloxham, J., 1996. The magnetic fields of Uranus and Neptune: methods and models. J. Geophys. Res. E Planets 101 (E1), 2177–2200. https://doi.org/10.1029/95JE03437.

Jackson, A., Jonkers, A.R.T., Walker, M.R., 2000. Four centuries of geomagnetic secular variation from historical records. Philos. Trans. R. Soc. A 358 (1768), 957–990. https://doi.org/10.1098/rsta.2000.0569.

Johnson, C.L., Constable, C.G., 1995. The time-averaged geomagnetic field as recorded by lava flows over the past 5Myr. Geophys. J. Int. 122 (2), 489–519. https://doi.org/10.1111/j.1365-246X.1995.tb07010.x.

Johnson, C.L., Constable, C.G., 1997. The time-averaged geomagnetic field: global and regional biases for 0-5 Ma. Geophys. J. Int. 131 (3), 643–666. https://doi.org/10.1111/j.1365-246X.1997.tb06604.x.

Korte, M., Donadini, F., Constable, C.G., 2009. Geomagnetic field for 0-3 ka: 2. a new series of time-varying global models. Geochem. Geophys. Geosyst. 10 (6) https://doi.org/10.1029/2008GC002297.

Korte, M., Constable, C., 2003. Continuous global geomagnetic field models for the past 3000 years. Phys. Earth Planet. Inter. 140 (1–3), 73–89. https://doi.org/10.1016/j.pepi.2003.07.013.

Matsushima, M., Honkura, Y., 1992. Reexamination of fluid motion in the earth's core derived from geomagnetic field data. -is the ω-effect really strong in the core? J. Geomagn. Geoelectr. 44 (7), 521–553. https://doi.org/10.5636/jgg.44.521.

Mound, J.E., Davies, C.J., 2023. Longitudinal structure of Earth's magnetic field controlled by lower mantle heat flow. Nat. Geosci. 16 (April) https://doi.org/10.1038/s41561-023-01148-9.

Nilsson, A., Suttie, N., Stoner, J.S., Muscheler, R., 2022. Recurrent ancient geomagnetic field anomalies shed light on future evolution of the South Atlantic Anomaly. In: , 119, pp. 1–7. https://doi.org/10.1073/pnas.2200749119.

Opdyke, N.D., Henry, K.W., 1969. A test of the dipole hypothesis. Earth Planet. Sci. Lett. 6 (2), 139–151. https://doi.org/10.1016/0012-821X(69)90132-0.

Panovska, S., Korte, M., Finlay, C.C., Constable, C.G., 2015. Limitations in paleomagnetic data and modelling techniques and their impact on Holocene geomagnetic field models. Geophys. J. Int. 202 (1), 402–418. https://doi.org/10.1093/gji/ggv137.

Panovska, S., Constable, C.G., Brown, M.C., 2018. Global and regional assessments of paleosecular variation activity over the past 100 ka. Geochem. Geophys. Geosyst. 19 (5), 1559–1580. https://doi.org/10.1029/2017GC007271.

Panovska, S., Korte, M., Constable, C.G., 2019. One hundred thousand years of geomagnetic field evolution. Rev. Geophys. 57 (4), 1289–1337. https://doi.org/10.1029/2019RG000656.

Shephard, G.E., Matthews, K.J., Hosseini, K., Domeier, M., 2017. On the consistency of seismically imaged lower mantle slabs. Sci. Rep. 7 (1), 1–17. https://doi.org/10.1038/s41598-017-11039-w.

Sprain, C.J., Biggin, A.J., Davies, C.J., Bono, R.K., Meduri, D.G., 2019. An assessment of long duration geodynamo simulations using new paleomagnetic modeling criteria (QPM). Earth Planet. Sci. Lett. 526, 115758 https://doi.org/10.1016/j.epsl.2019.115758.

Tarduno, J.A., Watkeys, M.K., Huffman, T.N., Cottrell, R.D., Blackman, E.G., Wendt, A., et al., 2015. Antiquity of the South Atlantic Anomaly and evidence for top-down control on the geodynamo. Nat. Commun. 6 https://doi.org/10.1038/ncomms8865.

Thébault, E., Finlay, C.C., Beggan, C.D., Alken, P., Aubert, J., Barrois, O., et al., 2015. International geomagnetic reference field: the 12th generation international geomagnetic reference field - the twelfth generation. Earth Planets Space 67 (1). https://doi.org/10.1186/s40623-015-0228-9.

Torsvik, T.H., Burke, K., Steinberger, B., Webb, S.J., Ashwal, L.D., 2010. Diamonds sampled by plumes from the core-mantle boundary. Nature 466 (7304), 352–355. https://doi.org/10.1038/nature09216.

Vandamme, D., 1994. A new method to determine paleosecular variation. Phys. Earth Planet. Inter. 85 (1–2), 131–142. https://doi.org/10.1016/0031-9201(94)90012-4.

Ziegler, L.B., Constable, C.G., 2015. Testing the geocentric axial dipole hypothesis using regional paleomagnetic intensity records from 0 to 300 ka. Earth Planet. Sci. Lett. 423, 48–56. https://doi.org/10.1016/j.epsl.2015.04.022.